SAG: Stars and Galaxies **Vol. 4**, id. 6, 2021 December 28

Distributions of dwarf galaxies around giant elliptical galaxies NGC 3923 and NGC 4636

Miyako Tozuka [1], Koji S. Kawabata [2], Yasushi Fukazawa [2], Shingo Nishiura [3], and Junko S. Hiraga [4]
[1]*Nishi-Harima Astronomical Observatory, Center for Astronomy, University of Hyogo, 407-2 Nishigaichi, Sayo-cho, Hyogo 679-5313, Japan*
[2]*Hiroshima University, 1-3-1 Kagamiyama, Higashihiroshima-shi, Hiroshima 739-8526, Japan*
[3]*Tokyo gakugei University, 4-1-1 Nukuikita-machi, Koganei-shi, Tokyo 184-8501, Japan*
[4]*Kwansei gakuinn University, 2-1 Gakuen, Sanda-shi, Hyogo 669-1337, Japan*
tozuka@nhao.jp

(Received 2021 October 14; accepted 2021 December 27)

Abstract

To obtain more information on the environment around elliptical galaxies, we observed the properties of dwarf galaxies around two giant elliptical galaxies, NGC 4636 and NGC 3923, using optical wide-field deep imaging. These galaxies have similar optical luminosities but have widely varying X-ray luminosities. We applied a convolution technique to detect low surface brightness objects, such as dwarf galaxies and used detection algorithms to identify groups of connected pixels exceeding a predetermined threshold above the background level. The well-observed radial profiles around NGC 4636 reveal that its dwarf galaxies are highly concentrated, especially its red dwarf galaxies. Although both NGC 4636 and NGC 3923 are similarly massive elliptical galaxies ($M > 10^{11}\,M_{\odot}$), based on gravitational mass profiles, NGC 4636 has a larger-scale potential structure than NGC 3923, with its dark matter surroundings becoming dominant. At a large distance of 300 kpc, NGC 4636 seems to have a deeper dark matter halo than NGC 3923, with a slightly higher number density of dwarf galaxies. In this work, our analyses obtained complete optical number density of dwarf galaxies around elliptical galaxies down to an absolute magnitude of $M_V = -15.5$ within 300 kpc, which is the region of dark matter dominance. Given that elliptical galaxies typically have an absolute magnitude of around $M_V = -22$ mag, the faint end corresponded to a stellar mass $\sim$ 1/1000 that of a giant elliptical galaxy, with a typical mass of $\sim 10^8\,M_{\odot}$. The number density of galaxies at $M_V = -15.5$ is 112.2 ± 65.21 Mpc^{-2} around the X-ray-bright NGC 4636 and 38.7 ± 36.15 Mpc^{-2} around the X-ray-faint NGC 3923. These values are lower than that of rich clusters of galaxies but higher than that of our local galaxy group that includes M31.

Key words: elliptical galaxies; dwarf galaxies; number density

1. Introduction

Optical observations can provide information on the brightness, color, spatial distribution, velocity, and elemental abundances of elliptical galaxies. Additionally, because elliptical galaxies emit hot interstellar medium (ISM), X-ray observations can give insights into the temperature and density distributions of plasma in such galaxies.

Giant elliptical galaxies contain a significant amount of hot ISM, with a plasma temperature of 10^6–10^7 K, meaning they are often X-ray-bright (Makishima et al. 2001; Fukazawa et al. 2006). ISM consists of accumulated lost stellar mass and supernova ejecta and is gravitationally bound by the galaxy potential (e.g., Forman et al. 1985; Matsushita 2001; Fukazawa et al. 2006). Therefore, ISM provides information on the galaxy's gravitational potential through the plasma's temperature and density distribution. Furthermore, ISM contains heavy elements (e.g., Matsushita 2001; Matsushita et al. 2003; Xu et al. 2002; Tozuka and Fukazawa 2008; Konami et al. 2014) possibly provided by stars; the confinement of heavy elements is related to galactic gravitational potential. Thus, ISM is important as it relates to both the chemical and dynamical evolution of elliptical galaxies and galaxy clusters.

One unresolved problem in X-ray observation is the large scatter of X-ray luminosities of giant elliptical galaxies with similar optical luminosities (Matsushita 2001; Boroson et al. 2011; Kim & Fabbiano 2013, 2015; Su et al. 2015; Goulding et al. 2016; Babyk et al. 2018). This scatter can be up to one order of magnitude even when optical luminosity is homogenous, indicating that ISM considerably differs in composition among galaxies with similar stellar masses and thus is related to galaxies' evolutionary histories. Extreme cases include overluminous elliptical galaxies that can have X-ray luminosities as high as that of a bright group of galaxies but that have a surrounding galaxy population with very poor X-ray luminosity (Matsushita 2001). This indicates the existence of galactic gravitational potentials that are as deep as

those of galaxy groups or poor clusters, and the presence of a large amount of dark matter binding to hot X-ray-emitting gases. The large scatter of X-ray luminosities can be attributed to the differences in ISM properties, and many studies have been attempted to resolve this issue. X-ray-bright elliptical galaxies are often at the low end of the gravitational potential of galaxy clusters and are thus embedded in the X-ray-bright intragroup medium (Eskridge et al. 1995; Makishima et al. 2001). In contrast, elliptical galaxies that are X-ray-faint are either isolated or at the peripheries of clusters. Therefore, an elliptical galaxy's X-ray luminosity is not strictly related to the number of surrounding galaxies. ASCA and ROSAT satellites show that X-ray isophotes of bright elliptical galaxies are larger than those of X-ray-faint ones (Matsushita et al. 1998; Matsushita 2001). Chandra's observations have also revealed that the radial profile of plasma temperatures in X-ray-bright galaxies exhibits a positive gradient toward the outer region, whereas that of X-ray-faint galaxies has a negative or flat gradient (Fukazawa et al. 2006). Gravitational mass profiles show that X-ray-faint galaxies contain their own dark matter with masses of 1.5–2 times greater than the stellar mass within 6 r_e. In contrast, X-ray-bright galaxies are in a larger-scale potential structure. This affects the gravitational potential profile of the galaxy itself, in turn leading to the differences in the temperature profile and X-ray ISM luminosity of X-ray-bright and X-ray-faint galaxies (Nagino & Matsushita 2009). The origins of these phenomena remain unresolved, especially regarding what creates the gravitational potential differences and how these galaxies differ in their evolution.

The universe's hierarchical structure is currently understood in terms of the cold dark matter (CDM) model, which predicts that several small objects evolve into a larger one through merging (Moore et al. 1999). In this paradigm, small subhalos are expected to exist around a massive galaxy even after evolution. Consequently, studies of dwarf galaxies around massive galaxies are crucial for obtaining a better understanding of CDM properties. In fact, many deep observations are being conducted near the Milky Way (Weisz et al. 2014) as well as in nearby rich clusters such as the Hydra I (Yamanoi et al. 2007), Coma (Yamanoi et al. 2012), and Centaurus clusters (Chiboucas & Mateo 2006). Current CDM theories are constrained by the faint-end slope of the luminosity functions (LFs) obtained when counting galaxies. Trentham and Tully (2002) found that LF depends on the environment and reflects galaxy formation and evolution history. The different faint-end slopes of LFs of elliptical galaxies in different X-ray environments provide insight into the differences in ISM properties relative to galaxy formation and evolution. Comparisons of LFs in different environments have been conducted, including comparisons between the inner and outer regions of clusters; between elliptical-rich cores and spiral-rich fields (Phillipps et al. 1998a, 1998b); between central and peripheral or field regions of galaxy clusters (Blanton et al. 2005; Popesso et al. 2006; Yamanoi et al. 2007); and among the center, intermediate region, and outskirts of a cluster (Yamanoi et al. 2012). However, no comparisons of LFs in different environments originating within galaxies exist. In this work, we compared the properties of dwarf galaxies distributed 300 kpc around two elliptical galaxies with different X-ray luminosities.

We also observed the color of these dwarf galaxies, which appears to correlate with the stars it contains. Some semi-analytical techniques of studying galaxy formation indicate that dwarf galaxy distribution and colors depend on the depth of the dark matter halo around the neighboring giant elliptical galaxy (Wang & Simon 2012; Wang et al. 2014; Sales et al. 2015).

2. Observations

We conducted deep optical observations of dwarf galaxies around two isolated giant elliptical galaxies, NGC 4636 and NGC 3923. As shown in Table 1, NGC 4636 and NGC 3923 show nearly identical optical B-band luminosity; however, the NGC 4636 has X-ray luminosity that is one order of magnitude brighter than NGC 3923. NGC 3923 is X-ray-faint, with a compact X-ray isophote and a small X-ray to optical luminosity ratio ($L_{\rm x} \,/\, L_{\rm B}$). In contrast, NGC 4636 is X-ray-bright, with hot gas extending beyond 100 kpc.

Both elliptical galaxies are isolated. NGC 4636 is a member of the Virgo cluster but is 10° south of the cluster's center, and no interactions have been observed. NGC 3923 is in a small group, and no interaction with that group has been observed. This indicates that both NGC 4636 and NGC 3923 are not affected by the gravitational potential of larger gravitating systems such as clusters of galaxies or neighboring galaxies. Thus, this provides an opportunity to compare the dwarf galaxy distributions around two elliptical galaxies with different X-ray luminosities.

We observed several positions around the two elliptical galaxies to map radial distributions up to $\gtrsim$ 300 kpc from each galaxy's center. Public data on isolated X-ray-faint galaxies are scarce. Although the Sloan Digital Sky Survey (SDSS)-IV data (Blanton et al. 2017) covers the X-ray-bright NGC 4636 area, the X-ray-faint NGC 3923 area has not been recorded. For comparison, obtaining data from NGC 4636 and NGC 3923 under the same conditions is necessary. The data used in this paper were obtained with a 2k-charge coupled device (CCD) camera attached to the 1.05 m Schmidt telescope at Kiso Observatory at the Institute of Astronomy, University of Tokyo, from January 2008 to July 2009. The camera has a back-illuminated SITe TK2048E CCD (2048 × 2048 pixels, 24 × 24 μm). The field of view (FoV) is $\sim 50' \times 50'$ with a scale of $1\farcs5$ pixel^{-1}. At a working temperature of 170 K, the CCD's dark count, ~ 1 e^{-1} h^{-1} pixel^{-1}, and readout noise (23 e^{-1} pixel^{-1}) are commonly negligible compared to the photon statistical noise of the object flux and sky background. On a dark night, the sky background flux was typically 21 and 18 mag arcsec^{-2} for the V and I bands, respectively.

A typical observation sequence for a single position consisted of 10–14 successive integrations with small telescope position offsets (four positions with $\Delta\alpha = \pm 1'$ and $\Delta\delta = \pm 1'$) through either a Johnson-Cousins V- or I- band filter. Each integration had an exposure time of 5 min. In the subsequent data reduction, we combined the acquired images for the same position and the same band using the shift-and-add method to minimize the harmful effects of bad pixels on the CCD. We deleted the effects of cosmic rays by combining images with various small offsets. Therefore, the total exposure time for a

Table 1. Basic properties of the two elliptical galaxies and field data.

Galaxy/Field	Position		D^{a}	$\log L_X^{b}$	$\log L_B^{c}$
	RA J_{2000}	DEC J_{2000}	(Mpc)	(erg s^{-1})	($L_{B\odot}$)
X-ray-bright Galaxy					
NGC 4636	$12^h42^m49.^s827$	+02°41′15.″99	15.92	41.59	10.51
X-ray-faint Galaxy					
NGC 3923	$11^h51^m01.^s694$	-28°48′21.″66	17.86	40.66	10.52
Field data[d]	$12^h29^m20^s$	+20°08′00″	–	–	–

[a] Distance (O'Sullivan et al. 2001).

[b] X-ray luminosity L_X (O'Sullivan et al. 2001).

[c] Optical B-band luminosity L_B (O'Sullivan et al. 2001).

[d] Field position neighboring the Virgo cluster observed for counting the number of field galaxies.

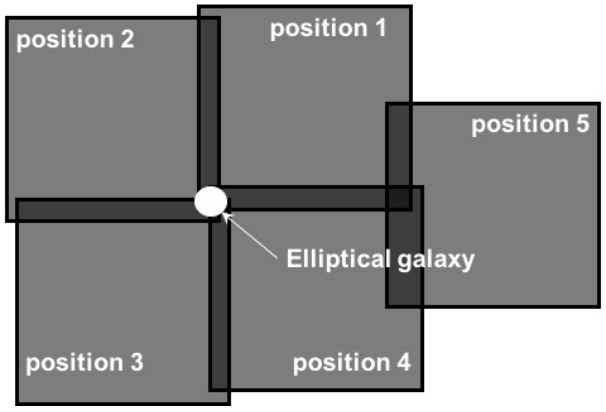

Fig. 1. Position offsets against the galaxy. $\Delta\alpha \simeq -20'$ and $\Delta\delta \simeq +20'$ for position 1, where $\Delta\alpha$ and $\Delta\delta \simeq \pm 20'$ are offsets along the right ascension the declination of the center of the field of view against the galaxy. $\Delta\alpha \simeq +20'$ and $\Delta\delta \simeq +20'$ for position 2, $\Delta\alpha \simeq +20'$ and $\Delta\delta \simeq -20'$ for position 3, and $\Delta\alpha \simeq -20'$ and $\Delta\delta \simeq -20'$ for position 4, and $\Delta\alpha \simeq -40'$ for position 5 as an outer region.

single position was typically 50–70 min.

To cover the $\sim 90' \times 90'$ field around the galaxy centers, we captured images at four positions (positions 1–4) with offsets of $\Delta\alpha = \pm 20'$ and $\Delta\delta = \pm 20'$ to the galaxy, which produces an overlapped field of $10' \times 10'$. Thus, we set the position to ensure that the center of the galaxy appeared in all frames, i.e., in the overlapped region (Figure 1). This four-region observation covers $\lesssim$ 200 kpc from the center of the galaxy. Thus, to enlarge the sample field, we captured images at one outer region ($\Delta\alpha = -40'$) as position 5 for both galaxies (Figure 1). Because of the large area of the image, a slight dithering movement generated translation and some rotation, meaning there are gaps of a few arcseconds in the overlapped region. We identified the identical objects in the two images when the difference in position between these two images was 5 arcsec and the magnitude difference was 0.1. We also rechecked these objects by eye. The resulting gaps are too small to affect the radial distribution. We adopted magnitude results from the image with the deepest limiting magnitude. Table 2 summarized the observational data.

Table 2 also shows the visible size and limiting magnitude of each position image. We could not obtain any significant data at position 3 because of our limited telescope time and poor weather conditions during the observations.

We also collected field data in addition to target data. We selected the genuine field region using the 2MASS Extended Sources Catalog (2MASX IPAC/UMass, 2003–2006). The region was separated from the center of the Virgo cluster by 447 kpc or $\Delta\alpha = +0.72°$ and $\Delta\delta = +7.41°$ from the center of the Virgo cluster, and the number density of galaxies approached an asymptotic value at the cluster outer limit (Figure 2).

3. Data Reduction and Analyses

Fixing the boundaries of stars and galaxies using the star-galaxy classifier of `SExtractor`[1] software was difficult because of bad seeing and a 1.5 arcsec pixel scale. Additionally, with a poor signal-to-noise ratio, the standard detection algorithm for the connected pixels sometimes fails to find extended objects with low surface brightness, such as dwarf galaxies. Consequently, we adopted a frequency domain technique described by Sabatini et al. (2003) to extract as many galaxies as possible from the objects SExtractor detected. This method is based on a convolution of images with matched filters, making it possible to use a galaxy's total flux instead of its very low local surface brightness.

3.1. First common process

We processed the data through a standard CCD data reduction method, mainly using IRAF[2], but also used

[1] SExtractor, "Source Extractor," free software for making a catalog of sources from astronomical images.(Bertin & Arnouts 1996)

[2] IRAF, "Image Reduction and Analysis Facility" which is distributed by the National Optical Astronomy Observatory (NOAO) and operated by the Association of Universities for Research in Astronomy (AURA) under a cooperative agreement with the National Science Foundation (NSF).

Table 2. Observation data

Galaxy/Field	Position[a]	$t_V^{\rm b}$ (min)	$t_I^{\rm b}$ (min)	Observation date (YYMMDD)	Seeing[c] (arcsec)	Limiting magnitude[d] V (mag)	I (mag)
Around X-ray-bright Galaxy NGC 4636							
	1	70	70	090719	5.3	16.9	16.9
	2	95	95	090720	2.9	17.8	17.8
	4	70	70	090719	3.8	18.8	18.7
	5	65	65	090719	3.9	18.7	19.2
Around X-ray-faint Galaxy NGC 3923							
	1	80	80	080114	4.8	18.3	17.9
	2	70	70	080429	4.3	18.0	17.5
	3	70	70	080430	3.3	17.4	17.7
	4	50	50	080507	3.7	17.1	16.6
	5	50	50	080507	3.5	18.9	19.1
Field data							
	–	80	80	080113	7.4	16.4	16.3

[a] Position offsets against the galaxy (See Figure 1).

[b] Total exposure times of the V and I bands, respectively.

[c] Radial profile fitting by a Gaussian model. Pixel scale is 1.5 arcsec

[d] The photometric error exceeds 0.1 mag in each field (see section 3.3.2)

`SExtractor`, `STSDAS`[3], and `HEASOFT`[4] software tools.

First, we de-biased and flat-fielded the obtained images. Bad pixels were masked at this stage (Figure 3). We then fitted and subtracted the background sky component of each image, making the sky level as flat as possible across the different offset images of crucial importance for detecting galaxies with low surface brightness such as dwarf galaxies. We fitted a low-order (second or third) two-dimensional function to the images. To obtain the background sky map, harmful fluctuations (e.g., bright stars and galaxies), which are pixels with two standard deviations ($2\,\sigma$) brighter than the sky background level, were replaced with linear interpolations along lines using the IRAF command "fixpix". We then performed a normal shift-and-add method to combine frames taken at the same position.

For calibration, we obtained dome flat-field images and bias frames. We performed the magnitude calibration using multiple (typically 20 in each position frame) stars listed in the AAVSO Photometric All Sky Survey (APASS) DR9 (Henden et al. 2016). We obtained the V- and I-band magnitudes of these stars from the APASS g'-, r'-, and i'-band magnitudes using the transformation equation of J.Allyn Smith et al. (2002).

3.2. Bright galaxies

Stars and bright galaxies can be easily detected with `SExtractor`. We assumed that every object (stellar and galactic) had more than 15 connected pixels and exceeded the ambient background fluctuation level by a factor of two. We distinguished between stellar objects and galaxies following criteria based on objects dimensions and peak flux described in Sabatini et al. (2003). This method has merit in that a change in image size within a frame due to aberration does not have much effect. Figure 4 shows the isophotal area as a function of surface isophotal flux weighted by the peak flux of objects detected in NGC 3923 position 3. The stellar locus (red points) and the region occupied by diffuse objects such as galaxies (green points) are visible; however, the stellar locus is not prominent. Thus, additional criteria are required to discriminate between stellar and diffuse objects.

As shown in the right panel of Figure 4, most of the detected objects were stellar objects, and their image sizes are comparable with the seeing size. We divided all data points into subsets consisting of 100 neighboring points along the vertical axis (i.e., 100 data points with similar surface isophotal flux values weighted by peak flux) and the derived mean and standard deviation (σ) values of each subset's isophotal area. However, data points were still insufficient to derive meaningful criteria. Therefore, we added an additional 100 neighboring points along the vertical axis (50 upper and 50 lower values) in each subset to calculate mean and σ. We then considered objects that had isophotal areas $2\,\sigma$ larger than the subset mean to be

[3] STSDAS, "Space Telescope Science Data Analyses System," prepared by the Space Telescope Science Institute (STScI) under the United States Government contract NAS5-26555.

[4] HEASOFT is supported by the High Energy Astrophysics Science Archive Research Center (HEASARC), which is the primary archive for NASA missions.

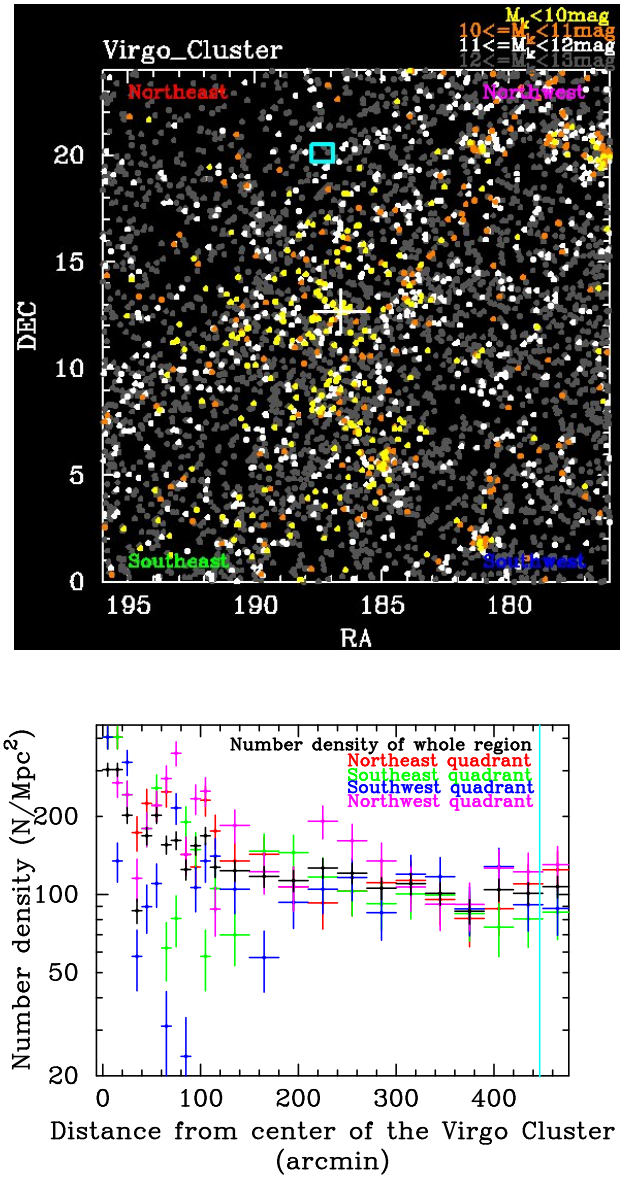

Fig. 2. Upper: Map of dwarf galaxies around the Virgo cluster from the 2MASS Extended Sources Catalog. The center of the Virgo cluster is at the center of this map. The blue square shows the region selected as our genuine field. This field located 447 kpc or $\Delta\alpha = +0.72°$ and $\Delta\delta = +7.41°$ from the center of the Virgo cluster. Lower: The number density distribution of dwarf galaxies versus distance from the center of the Virgo cluster, as deduced from the left panel. The density distribution of the whole region is shown in black. The number density of each quadrant is shown in a different color. The vertical blue line indicates the position of the genuine field.

diffuse objects, i.e., a galaxy.

To identify bright galaxies, we adopted the photometric parameters derived by `SExtractor` and calibrated those parameters relative to the standard star observations.

3.3. Faint galaxies

3.3.1. Masking stars and bright galaxies

Before detecting low surface brightness objects, such as faint galaxies, we must mask high-count objects in advance. This greatly reduces mis-sampling of faint galaxies in the later process. First, we prepared the object image and corresponding sky background image derived through low-order function fitting (see section 3.2). Second, we identified galaxies brighter than $V = 16$ mag and all stellar objects and then derived their radii at which the flux fell within $1\,\sigma$ of sky noise from the `SExtractor` calculations. Third, we masked each object by replacing it with a corresponding circular region of the sky background image with the object radius. With this, we obtained masked images.

However, this masking procedure decreases the number of galaxies in the dataset due to the loss of usable area for galaxy detection, which would lead to fewer faint galaxies counted. We will simulate and evaluate this effect later.

3.3.2. Convolution by multiscale filter

We adopted a sophisticated convolution method developed by Sabatini et al. (2003) to detect faint and diffuse galaxies. Our procedure was essentially the same as that described in sections 4.3–4.4 of Sabatini et al. (2003), except for the negative region of the filter function, which is not described in their paper. The filter we defined consists of an object with an exponential brightness distribution ($F_* \propto \exp[-r/(3\alpha)]$, at $r \leq 3\alpha$) and a doughnut-like region with negative values ($\propto -\exp(-r)$ at $3\,\alpha < r \leq 6\,\alpha$). Thus, this function is zero at $r = 3\,\alpha$ and $r \geq 6\,\alpha$. The full-width at half-maximum (FWHM) of the filter can be approximated with $1\,\alpha$, and the typical size of the object is represented by the scale size ($H = 3\,\alpha$). We adopted many filter sizes, ranging from $\alpha = 1.5''$ (corresponding to the typical seeing size) to $\alpha = 12''$ (corresponding to 1 kpc at the Virgo cluster) with a $0.1''$ step, to match various objects. Each filter was scaled and adjusted to give zero for blank sky areas.

After performing convolution for the cleaned images with the filter combinations, we built a significance image which had a pixel value equal to the maximum value among the series of convolution images. On a different array with the same dimensions as the significance image, we saved the filter scale α on which the maximum value was found (i.e., α of the best-matched filter), which serves as an estimate of the object's radius. We then detected galaxy candidates by taking all peaks above the $3\,\sigma$ threshold in the significance image. When the scale size of filter H matched the scale size of galaxy h ($h \simeq H = 3\,\alpha$ in the significance image), the value of the convolution can be represented as follows:

$$I = \int f_0 \mathrm{e}^{-\mathrm{r/h}} (\mathrm{F}_* \mathrm{e}^{\mathrm{r/H}})\, 2\pi \mathrm{r dr} = \frac{\mathrm{F}_*}{2} \pi \mathrm{f}_0 \mathrm{h}^2, \quad (1)$$

where $f_0 \mathrm{e}^{-\mathrm{r/h}}$ is the assumed exponential profile of the galaxy and $F_* \mathrm{e}^{-\mathrm{r/H}}$ is the positive part of the filter.

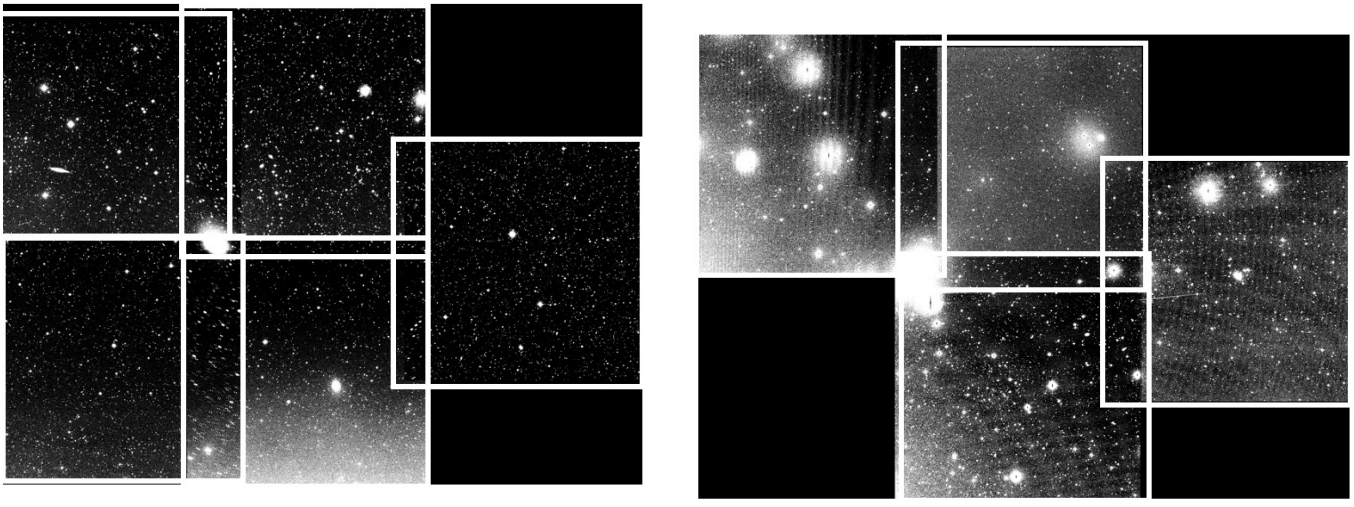

Fig. 3. Combined V-band image of X-ray-bright elliptical galaxies NGC 3923 (left) and NGC 4636 (right). For good contrast, images include the background sky component.

We can then estimate surface brightness at the center of the object in the original image as follows:

$$f_0 = \frac{I}{2\pi h_{\rm best}^2 F_*}. \quad (2)$$

To confirm the reliability of these calculations, we show f_0 derived by this method against the peak brightness derived by normal aperture photometry in Figure 5. As shown in the figure, the two are consistent.

We performed magnitude calibration as follows. First, we selected several galaxies with modest brightness (i.e., galaxies that were not masked in the cleaned image) detected by `SExtractor`. We then calibrated the magnitudes of these galaxies with the same method used for bright galaxies. Next, we compared those magnitudes against their peak V value in the significance image, which is shown in Figure 6. Using this relationship, we derived the magnitude of all candidate galaxies. We estimated the limiting magnitude of the detection to be the magnitude where the photometric error determined by `SExtractor` results exceeded 0.1 mag in each field.

3.4. Contamination by false and background galaxies

The convolution method described above finds many dwarf galaxies, with a typical number of galaxies detected in each image ($45' \times 45'$, neglecting the edge of the FoV due to an incomplete convolution process) reaching $\sim 10^2$. However, it remains unclear how well the procedure works for less luminous, diffuse galaxies. Furthermore, a non-negligible fraction of these detected galaxies may be background galaxies.

To test the detection reliability and measure the completeness of contamination by false or background galaxies, we performed a simulation using an artificial image that mimicked Virgo cluster observation. To the image, we added cluster members following the Schechter luminosity distribution, background galaxies following the power-law luminosity distribution, stars within our own galaxy, and typical background sky counts with Poisson noise. We then reduced the artificial image using the same methods as the observation data.

We found that background galaxy contamination was negligible ($< 2\%$), as our masking procedure would reject most background galaxies as stars and because the scale length was small. This is consistent with the numerical estimation of Sabatini et al. (2003). As another estimation of background galaxy contamination, we observed the field position of the Virgo cluster (see section 2) and counted the dwarf galaxies using the same method. We detected only a few galaxies in each FoV, which is consistent with the test results. Figure 7 shows the detection completeness estimated by our simulation. In the artificial image, the limiting magnitude ($\sigma = 0.1$ mag) is $V = 19.4$ mag. There was a significant loss of detection for galaxies equal to or fainter than the limiting magnitude of the observation. Thus, discussing such faint galaxies in our data is undoubtedly difficult. In contrast, the detection was almost complete at $V < 16.5$ mag. In the following section, we discuss galaxies brighter than $V < 16.5$ mag, which corresponds to absolute magnitude values $M_V = -14.99$ for NGC 4636 and $M_V = -15.07$ for NGC 3923.

4. Results and Discussion

We obtained the number density of dwarf galaxies around giant elliptical galaxies down to an absolute magnitude of $M_V = -15.5$. As the typical absolute magnitude of a giant elliptical galaxy is approximately $M_V = -22$ mag, our faint end of galaxy brightness corresponds to $\sim$ 1/1000 of a giant elliptical galaxy with a mass of $\sim 10^8\, M_\odot$. Such a deep survey of areas around elliptical galaxies in low galactic latitudes remains insufficient. Although the SDSS-IV data (Blanton et al. 2017) covers the area around NGC 4636, areas around X-ray-faint regions, such as NGC 3923, have yet to be recorded.

We individually analyzed V- and I-band data and then compiled them with cross-correlation of both band samples. In

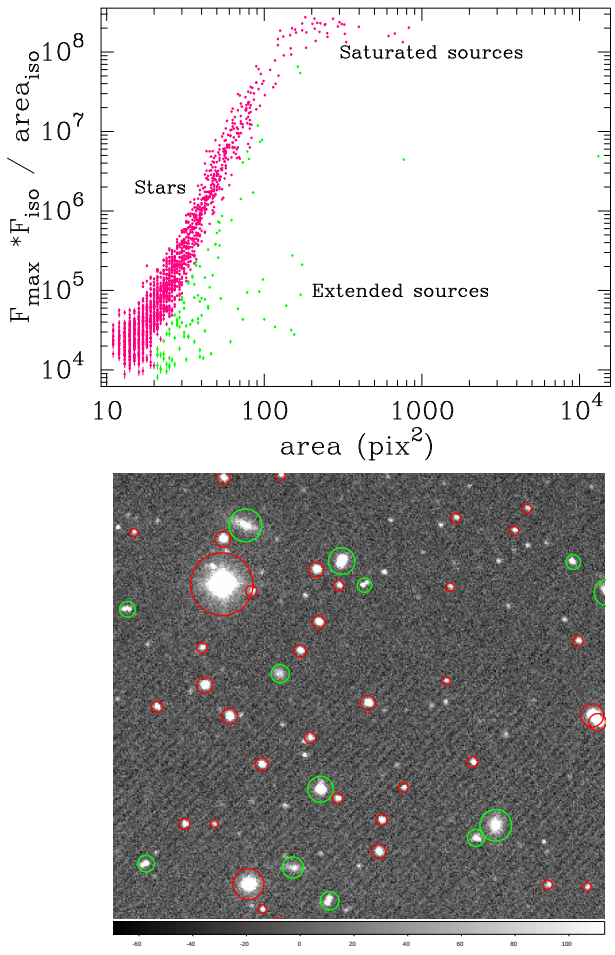

Fig. 4. Upper: Surface isophotal flux weighted by the peak flux is plotted versus the isophotal area of NGC 3923 position1 data in the V-band. There is a clear locus of the stellar samples. Using a curve fitted to this stellar locus, we can distinguish stars and galaxies. Lower: Region of NGC 3923 and the detection of normal objects. Red circles denote stellar objects, and green circles denote galaxy samples.

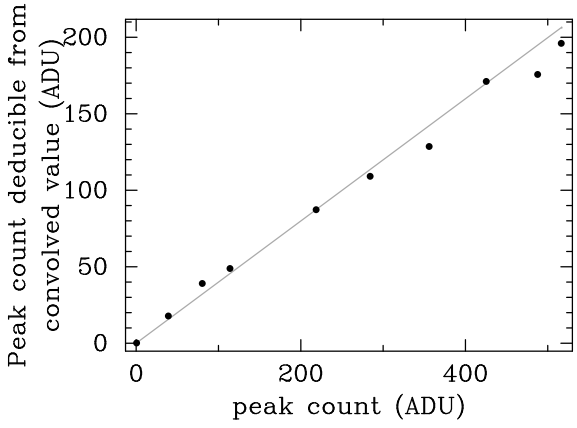

Fig. 5. Comparison of the peak value of the significance image with that of the raw image.

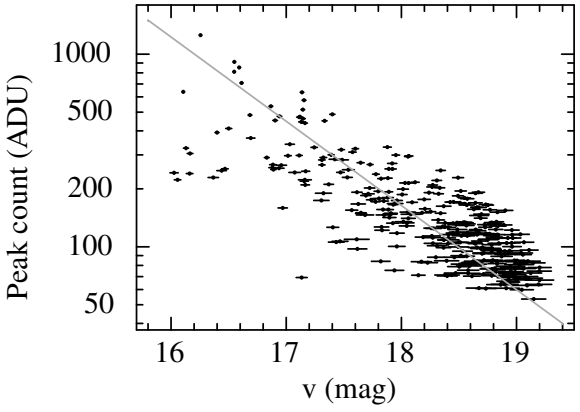

Fig. 6. Relationship between the peak V value of the significance image and the magnitudes obtained by `SExtractor` for the detected galaxies.

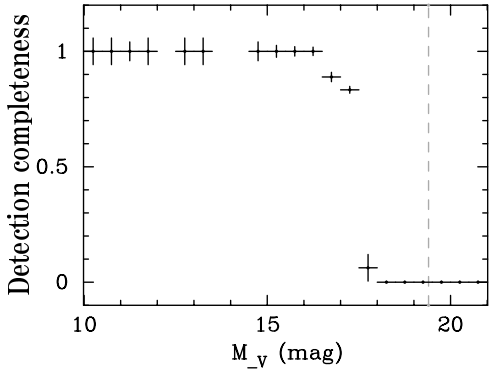

Fig. 7. Detection completeness of galaxies estimated using an artificial image. The gray dashed line shows the limiting magnitude (19.4 mag). There was a loss in detection completeness for galaxies brighter than the limiting magnitude because the artificial image contains no galaxies at this magnitude.

other words, we included only galaxies that had been detected in both bands and also checked the detected galaxies by eye. Figure 8 shows the galaxies adopted as a sample around NGC 3923 (left) and NGC 4636 (right).

Figure 9 shows that the radial number density distribution of dwarf galaxies is almost constant in the outer region and increases toward the center within 100 kpc. Our sample of dwarf galaxies contains three components: a component consisting of the giant elliptical galaxy (galaxy component), a uniform field component of the sky (field component), and a component associated with the ambient group of galaxies around the giant elliptical galaxy, which has a larger structure than the giant elliptical galaxy (group component). Therefore, we should consider the field and the group components.

For the field component, we observed one region 7° northeast from the center of the Virgo cluster, as described in section 2. In Figure 9, the black data represent the total component after data reduction and the gray data represent the field compo-

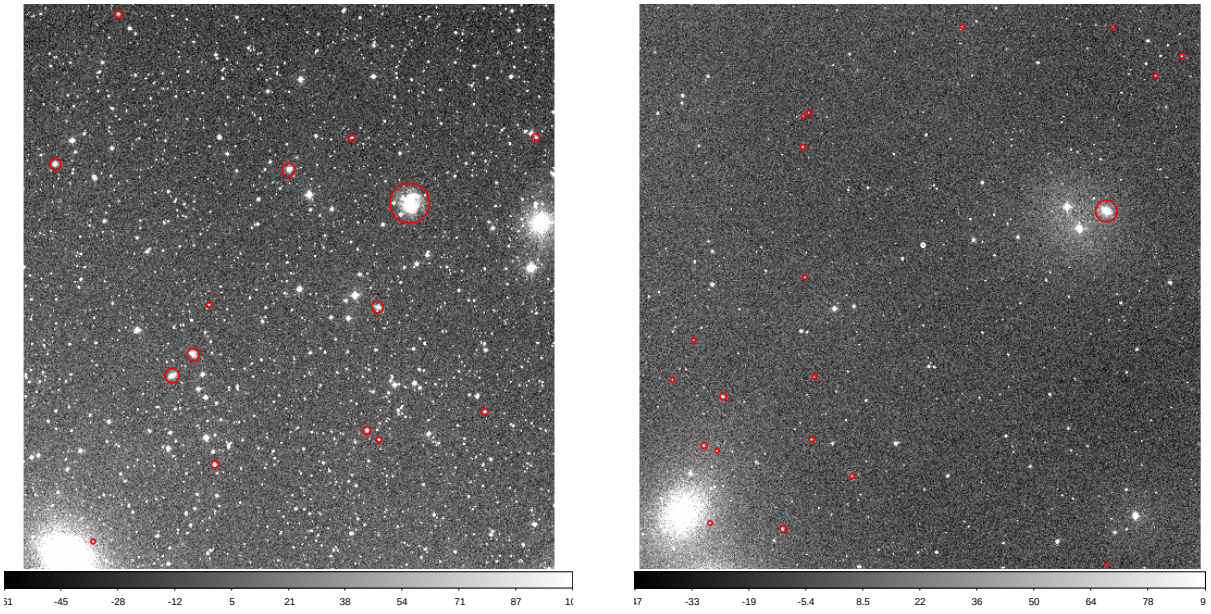

Fig. 8. Final samples of dwarf galaxies were detected in one region (which shows about 50 × 50 arcmin cutouts). The upper side of the images shows the north direction and the left side shows the east direction around NGC 3923 (left) and NGC 4636 (right). Red circles denote the detected dwarf galaxies in each region. The limiting magnitude of the NGC 3923 region is $V = 18.3$ mag, and that of the NGC 4636 region is $V = 18.8$ mag.

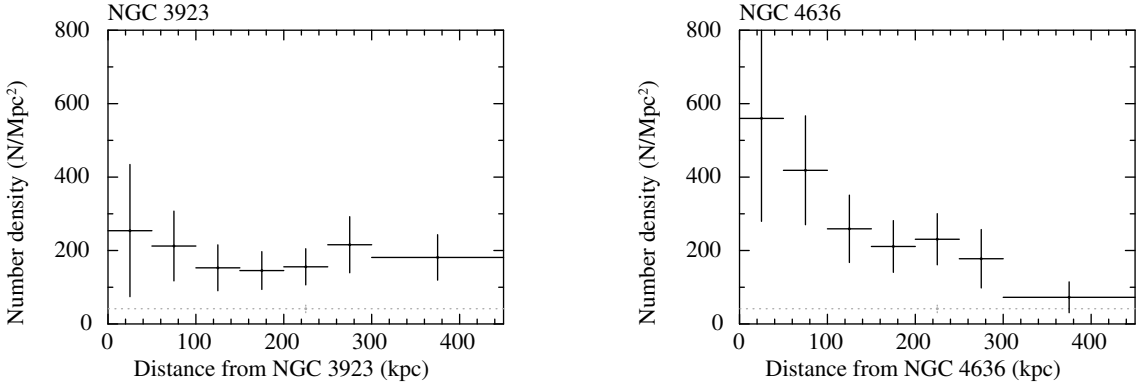

Fig. 9. Number density of dwarf galaxies as a function of their distances from the elliptical galaxy. The black data represent the total component, and the gray dots data are the results after subtracting the field component.

nent. The field component is 41.5 ± 23.97 Mpc^{-2}; therefore, the number densities of dwarf galaxies in these plots are higher than the field components.

Regarding the group component, Ferguson and Sandage (1990) surveyed galaxies more than 1 Mpc from the center of five nearby groups of galaxies and reported that the radial distribution of galaxies well fit the King model, which has core radii of 200–700 kpc.

Therefore, the constant component of dwarf galaxy density more than 300 kpc from the galaxy cluster center can be explained by the group component if the giant galaxy has a core radius > 300 kpc. Figure 10 shows the number density of dwarf galaxies as a function of M_V within 300 kpc.

Next, we divided NGC 4636 and NGC 3923 into red and blue distributions at $V - I = 0.2$. Figure11 shows color-magnitude diagrams of dwarf galaxies in the observed regions of NGC 3923 and NGC 4636. Using $V - I \geq 0.2$, we separated the galaxies around NGC 4636 into approximately two equal parts. In this analysis, $V - I \geq 0.2$ corresponds to the distribution of red dwarf galaxies and $V - I < 0.2$ corresponds to that of blue dwarf galaxies.

Figure 12 shows the number density of dwarf galaxies as a function of distance from parent elliptical galaxies. Each number density is what remains after subtracting the average number density at 350–450 kpc as the group component includes the field component. The black line indicates the remainder after subtracting the group component from the total component. These results reveal previously undetected and much redder dwarf galaxies concentrated around NGC 4636. Contrastingly, NGC 3923 showed a much weaker concentration. Some previous research (Wang et al. 2014; Sales et al. 2015) indicated that the satellite populations around NGC 3923 and NGC 4636 within 0.2 virial radii, which corresponds to hundreds of kpc, were similar because they have similar stellar

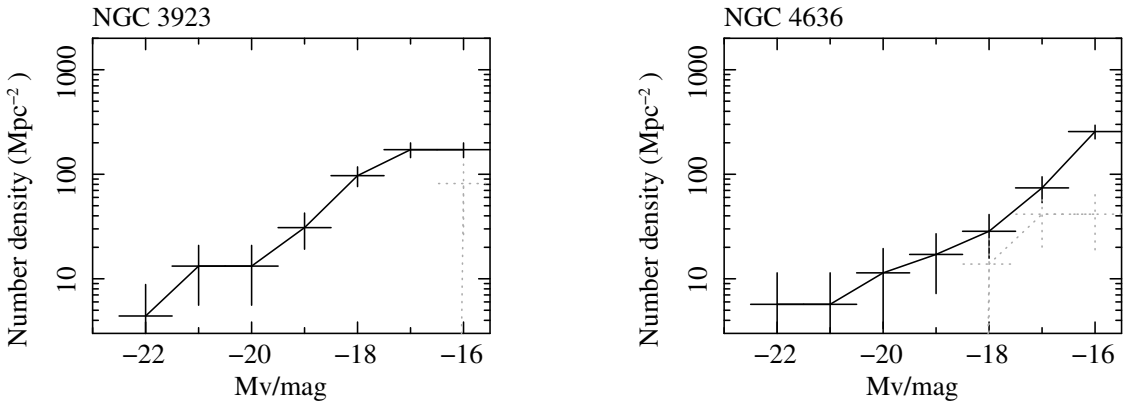

Fig. 10. Number density of dwarf galaxies as a function of absolute magnitude (M_V). The black data represent the total component, and the gray dot data are the field component results.

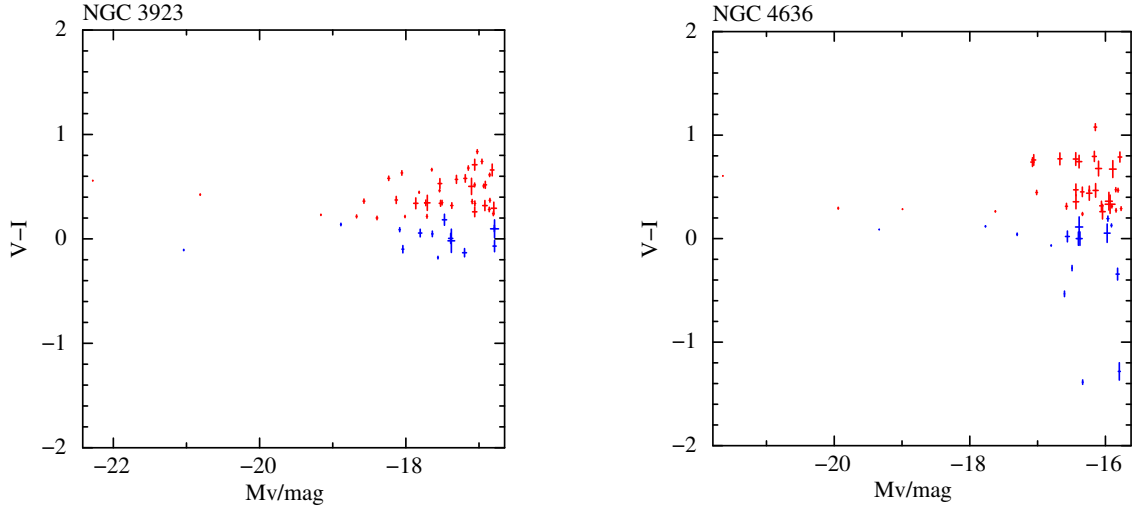

Fig. 11. Color-magnitude diagrams of NGC 3923 (left) and NGC 4636 (right). Red data represent the distribution of red dwarf galaxies ($V - I \geq 0.2$). Blue data represent the distribution of blue dwarf galaxies ($V - I < 0.2$)

masses. Both NGC 4636 and NGC 3923 are massive elliptical galaxies ($M > 10^{11}\,M_{\odot}$), and for the most massive elliptical galaxies, red satellites galaxies dominate and tend to be more steeply distributed than bluer ones.

These profiles of dwarf galaxies, including red dwarf galaxies around NGC 4636, agree with the semi-analytical techniques of Wang and Simon (2012), Wang et al. (2014), and Sales et al. (2015). Although NGC 3923 and NGC 4636 have comparable optical luminosities, NGC 4636 has a higher gravitational mass than NGC 3923 based on X-ray observation (Nagino & Matsushita 2009). Only two examples with large systematic error exist to date; therefore, systematic observation of these tendencies for other elliptical galaxies is required for further discussion.

Figure 13 also shows number densities of dwarf galaxies as a function of magnitude. These number densities are the remainder after subtracting the average number density at 350 to 450 kpc, where the group component includes the field component. Data on the color of these dwarf galaxies do not appear because of large systematic error.

Our results indicate that the typical number density of galaxies is 112.2 ± 65.21 Mpc^{-2} around NGC 4636 and 38.7 ± 36.15 Mpc^{-2} around NGC 3923 at $M_V = -15.5$. These values are lower than that of nearby rich clusters of galaxies, including the Hydra I cluster (Yamanoi et al. 2007), which has approximately 300 Mpc^{-2} in the B-band and 600 Mpc^{-2} in the R-band; the Coma cluster (Yamanoi et al. 2012), with approximately 200 Mpc^{-2} in the R-band; and the Centaurus cluster (Chiboucas & Mateo 2006), which has approximately 160 Mpc^{-2} in the V-band after correction for background contamination. On the other hand, this value is higher than that of our local galaxy group including M31, which has 2 Mpc^{-2} at $M_V = -15.5$ (Weisz et al. 2014).

We also found a slight difference in the number density be-

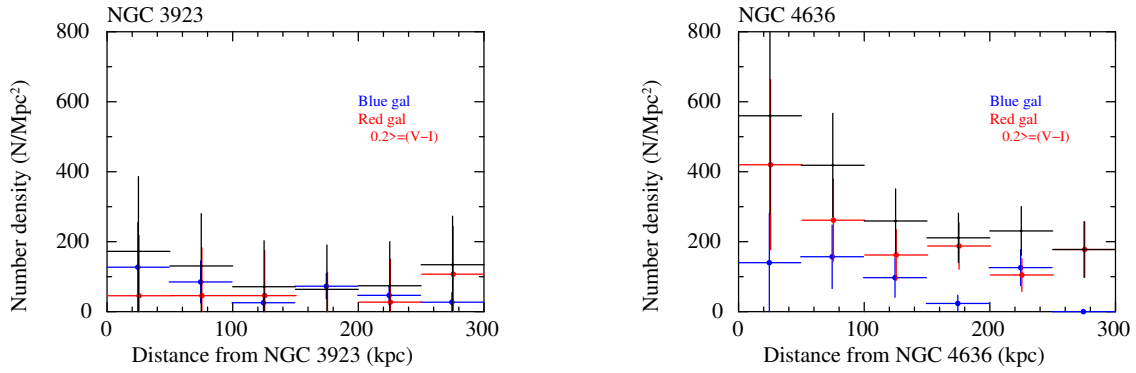

Fig. 12. Number density of dwarf galaxies as a function of distance from the parent elliptical galaxy. Each number density is what is left after subtracting the average number density at 350–450 kpc as the group component including the field component. The black line shows the remainder after subtracting the group component from the total component. The red line is the distribution of red dwarf galaxies ($V - I \geq 0.2$). The blue line is the distribution of blue dwarf galaxies($V - I < 0.2$)

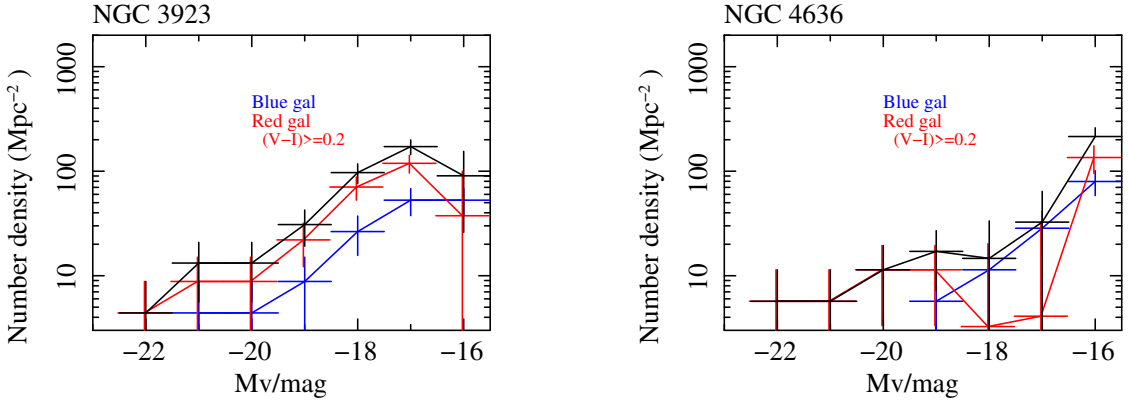

Fig. 13. Number density of dwarf galaxies as a function of a magnitude of V. Number density is the remainder after subtracting the average number density at 350–450 kpc as the group component including the field component. Data on the color of dwarf galaxies do not appear to large systematic error.

tween NGC 4636 and NGC 3923. Nagino and Matsushita (2009) indicated that NGC 4636 has a higher gravitational mass than NGC 3923 at over 6 r_e, which corresponds to 45.0 kpc for NGC 4636 and 27.6 kpc for NGC 3923. Previous research (Wang et al. 2014; Sales et al. 2015) also indicated that satellite galaxies roughly follow the distribution of dark matter in a distance range of 0.2–1 virial radii, which corresponds to several hundreds of kpc and includes in the outer regions where dark matter dominates (Schuberth et al. 2006; Schuberth et al. 2012; Norris et al. 2012). Although we found no obvious evidence of a relationship between the number density of satellite galaxies and the dark matter halo of elliptical galaxies, NGC 4636 appears to have a deeper dark matter halo than NGC 3923 and has a slightly higher number density of dwarf galaxies than NGC 3923. However, a more detailed discussion will require better velocity dispersion.

5. Conclusion

We observed the properties of dwarf galaxies around two examples of elliptical galaxies, NGC 4636 and NGC 3923, to obtain more information on the environment around elliptical galaxies. NGC 4636 and NGC 3923 have similar optical luminosities, which are used to calculate component stellar mass, but have different X-ray luminosities, which can be used to calculate total mass. Thus, both NGC 4636 and NGC 3923 have similar stellar masses but NGC 4636, which is X-ray-bright, has a higher gravitational mass. When we observe the environment around elliptical galaxies to greater distances, we can determine not only stellar mass but also the total gravitational mass.

Both NGC 4636 and NGC 3923 are similarly massive elliptical galaxies ($M > 10^{11} M_{\odot}$). On the other hand, based on their gravitational mass profiles NGC 4636 contains a larger-scale potential structure than NGC 3923 both within and over 6 r_e (Nagino & Matsushita 2009). In the outer regions, dark matter dominates (Schuberth et al. 2006, 2012; Norris et al.

2012). Previous research (Wang et al. 2014; Sales et al. 2015) also indicated that satellite galaxies roughly follow the distribution of dark matter in a distance ranging from 0.2 to 1 virial radii. Comparing NGC 4636 to NGC 3923 at large 300 kpc distances, NGC 4636, which seems to have a deeper dark matter halo than NGC 3923, shows a slightly higher number density of dwarf galaxies than NGC 3923. Dwarf galaxies are also observed to be more highly concentrated around NGC 4636. More information on the dispersion velocity of dwarf galaxies is required to better understand the dynamic equilibrium processes of elliptical galaxies. Therefore, systematic observation of these tendencies for other elliptical galaxies is required for further discussion.

Although the SDSS-IV data (Blanton et al. 2017) cover an area of 200–700 kpc around the NGC 4636, areas around X-ray-faint galaxies, such as NGC 3923, have yet to be analyzed. We obtained the number density of dwarf galaxies around both elliptical galaxies down to an absolute magnitude of $M_V = -15.5$. Given that the typical absolute magnitude of elliptical galaxies is around $M_V = -22$ mag, the faint end corresponded to a stellar mass $\sim$ 1/1000 that of a giant elliptical galaxy or a galaxy mass of $\sim 10^8\,M_\odot$. The observed radial profile around the NGC 4636 revealed its satellite dwarf galaxies were relatively concentrated, especially its red dwarf galaxies. We also found a slight difference in the galaxy number density between NGC 4636 and NGC 3923 within a radius of approximately 300 kpc. The typical number density of galaxies at $M_V = -15.5$ around NGC 4636 is 112.2 ± 65.21 Mpc^{-2}, whereas it is 38.7 ± 36.15 Mpc^{-2} around NGC 3923. These values are lower than that of the nearby rich cluster of galaxies but higher than that of our local groups including M31.

6. Acknowledgement

Finally, we are grateful to the referees for their helpful comments. The authors also thank members of the Kiso observatory for the opportunity of our observation.

References

Babyk, I. V., McNamara, B. R., Nulsen, P. E. J., Hogan, M. T., Vantyghem, A. N., Russell, H. R., Pulido, F. A., & Edge, A. C. 2018, ApJ, 857, 32
Bertin, E., & Arnouts, S. 1996, A&A, 117, 393
Blanton, R. M., Eisenstein, D., Hogg, W. D., Schlegel, J.D., & Brinkmann, J. 2005, ApJ, 629, 143
Blanton, R. M., et al. 2017, AJ, 154, 28
Boroson, B., Kim, D., & Fabbiano, G. 2011 , ApJ, 729, 12
Chiboucas, K., & Mateo, M. 2006, AJ, 132, 347
Eskridge, P. B., Fabbiano, G., & Kim, D. 1995, AJ, 441, 523
Ferguson, C. H., & Sandage, A. 1990, AJ, 100, 1
Forman, W., Jones, C., & Tucker, W. 1985, ApJ, 293, 102
Fukazawa, Y., Botoya-Nonesa, G. J., Pu, J., Ohto, A.,& Kawano, N. 2006, ApJ, 636, 698
Goulding, D. A., et al. 2016, ApJ, 826, 167
Henden, A. A., Templeton, M., Terrell, D., Smith, T.C., Levine, S., & Welch, D. 2016,VizieR Online Data Catalog
Kim, D., & Fabbiano, G. 2013, ApJ, 776, 116
Kim, D., & Fabbiano, G. 2015, ApJ, 812, 127
Konami S., Matsushita, K., Nagino, R., & Tamagawa, T. 2014, ApJ, 783, 8
Makishima, K., et al. 2001, PASJ, 53, 401
Matsushita, K., Makishima, K., Ikebe, Y., Rokutanda, E., Yamasaki, Y. N., & Ohashi, T. 1998, ApJ, 499, L13
Matsushita, K. 2001,ApJ, 547, 693
Matsushita, K., Finoguenov, A., & Böhringer, H. 2003, A&A, 401, 443
Moore, B., Ghigna, S., Governato, F., et al. 1999, ApJ, 524,19
Nagino, R., & Matsushita, K. 2009, A&A,501,157
Norris, A. M., et al. 2012, MNRAS, 421, 1485
O'Sullivan, E., Forbes, A. D.,& Ponman, J. T. 2001, MNRAS, 328, 461
Phillipps, S., Parker, A. Q., Schwartzenberg, M. J., & Jones, B. J. 1998, ApJ, 493, L59
Phillipps, S., Driver, P. S., Couch, J. W., & Smith, M. R. 1998, ApJ, 498, L119
Popesso, P., Biviano, A., Böhringer, H., & Romaniello, M. 2006, A&A, 445, 29
Sabatini, S., Davies, J., Scaramella, R., Smith, R., Base, M., Linder, M. S., Roberts, S.,& Testa, V. 2003, MNRAS, 341, 981
Sales, V. L., et al. 2015, MNRAS, 447, L6
Schuberth, Y., Richtler, T., Dirsch, B., Hilker, M., Larsen, S.S., Kissler-Patig, M.,& Mebold, U. 2006, A&A, 459, 391
Schuberth, Y., Richtler, T., Hilker, M., Salinas,R., Dirsch, B.,& Larsen, S. S. 2012, A&A, 544, A115
Allyn Smith, J., et al. 2002, AJ, 123, 2121
Su, Y., Irwin, A. J., White III, E. R., & Cooper, M. C. 2015, ApJ, 806, 156
Tozuka, M.,& Fukazawa, Y. 2008, PASJ, 60, 527
Trentham, N.,& Tully, B. R. 2002, MNRAS, 335, 712
Weisz, R. D., Dolphin, E. A., Skillman, D. E., Holtzman, J., Gilbert, M. K., Dalcanton, J. J.,& Williams, F. B. 2014, AJ, 789, 147
Wang, W., & White, M. D. S. 2012, MNRAS, 424, 2574
Wang, W., Sales, V. L., Henriques, B. M. B., & white, M. D. S. 2014, MNRAS, 442, 1363
Xu, h. et al. 2002, ApJ, 579, 600
Yamanoi, H. et al. 2007, AJ, 134, 56
Yamanoi, H. et al. 2012, AJ, 144, 40